

# Flow Field Visualization in Structured Packing Using Real Time X-ray Radiography

Scott A. Owens,\* Andreas Kossmann, John Farone, and R. Bruce Eldridge

*Process Science and Technology Center, University of Texas, Austin, Texas 78712*

Richard A. Ketcham

*Jackson School of Geosciences, University of Texas, Austin, Texas 78712*

This research developed an experimental method for validating the CFD representation of single-phase (vapor) flow through structured packing. Real time X-ray radiography was used to visualize fluid streamlines in structured packing by tracking neutrally buoyant X-ray absorbing particles entrained in water flow. Flow through the packing was found to be uniform, whereas flow at the packing element joints exhibited chaotic flow and recirculation zones. Individual radiographs were analyzed to determine particle displacement and compute local velocities. This data could be used to validate existing computational fluid dynamics (CFD) models, including fluids other than water through the use of similarity theory.

## 1. Introduction

**1.1. Motivation.** Fluid flow impacts the performance of process systems in a broad cross-section of industrial applications. Separations equipment, chemical reactors, biological contactors, fermentation vessels, and heat transfer devices all perform at the mercy of hydraulic phenomena. In spite of the high energy required for distillation, it is often chosen over other separation processes because of the relatively low initial capital investment, flexibility, and ability to yield high-purity products. Currently, every barrel of crude oil is subjected to an initial separation by distillation, and nearly every chemical process requires distillation for product recovery or purification. Because of high initial capital costs, alternative technologies are not likely to be implemented until existing distillation columns require replacement. Substantial cost savings can be achieved by relatively small process efficiency improvements in distillation column operation and column internal design. Structured packing is the current state-of-the-art contactor internal. A thorough understanding of the internal flow dynamics of an operating vapor–liquid contactor will be required to design next-generation column internals.

Historically, models of the flow fields have been, at best, highly empirical. With the advent of high-speed computers utilizing efficient parallel processing architectures, detailed computer simulations of hydraulics have become feasible. However, the ability to validate these high-fidelity models has lagged behind the model development. With the help of X-ray imaging, flow fields in structured packed columns can be made visible and are therefore available for comparison with CFD models. Validating and improving these models is of great interest as distillation is a low thermal efficiency unit operation that currently accounts for 40% of the processing energy consumed in refining and continuous chemical processes.

CFD codes are rapidly becoming a more and more powerful tool in all engineering fields. The speed of computational advancement has opened up a gap between developing new models for CFD simulations and actually validating those models. In general, CFD codes cannot be a trusted independent source until the codes have been thoroughly confirmed. For validation of CFD codes,

there are several different approaches. Laser doppler velocimetry was the first widely used technique to validate CFD code, whereas particle image velocimetry and particle tracking velocimetry have gained widespread usage recently.<sup>1–10</sup> Though there are many variations to these techniques, they are predominately optically based so that limitations remain. These limitations can be avoided by using X-ray imaging. Medical X-ray technology has been used for obtaining a real time movie of flow in a human subject. Cardiac artery flow studies are a prime example. These studies typically involve injecting a dye into a flowing stream and watching the dye position change with time. This research extends this technology to an industrial application. X-ray attenuating neutrally buoyant particles following the streamlines are introduced into a column and traced over time thus resulting in a movie. The movie results then can be analyzed and compared to CFD simulations.

This research shows a method by which empirical data can be obtained for validation against CFD simulations. This article covers the selection and construction of an experimental apparatus that allowed neutrally buoyant, lead-core foam particles to be injected upstream of a column containing structured packing. The particles' path through the packing was tracked in two dimensions via a cone-beam, X-ray emitter and area detector. Data in the form of position as a function of time was obtained directly. This data was then interpreted to give macroscopic views of path lines and local velocity vectors, which can be directly compared with similar data generated by CFD simulation.

**1.2. Attenuation.** As X-rays pass through an object, they are attenuated via both scattering and absorption. The attenuation of an X-ray passing through a homogeneous material is governed by Beer's Law:

$$I = I_0 \exp[-\mu x] \quad (1.1)$$

where  $I_0$  is initial X-ray intensity,  $\mu$  is the linear attenuation coefficient (units: 1/length), and  $x$  is the length of the X-ray path.<sup>11</sup> If the scan object is composed of a number of different materials, the equation becomes:

$$I = I_0 \exp \left[ \sum_i (-\mu_i x_i) \right] \quad (1.2)$$

where each increment  $i$  reflects a single material with attenuation coefficient  $\mu_i$  over a linear distance  $x_i$ .<sup>11</sup> To take into account the

\* To whom correspondence should be addressed. Tel.: (512) 471-1807. Fax: (512) 471-1720. E-mail: sao293@che.utexas.edu.

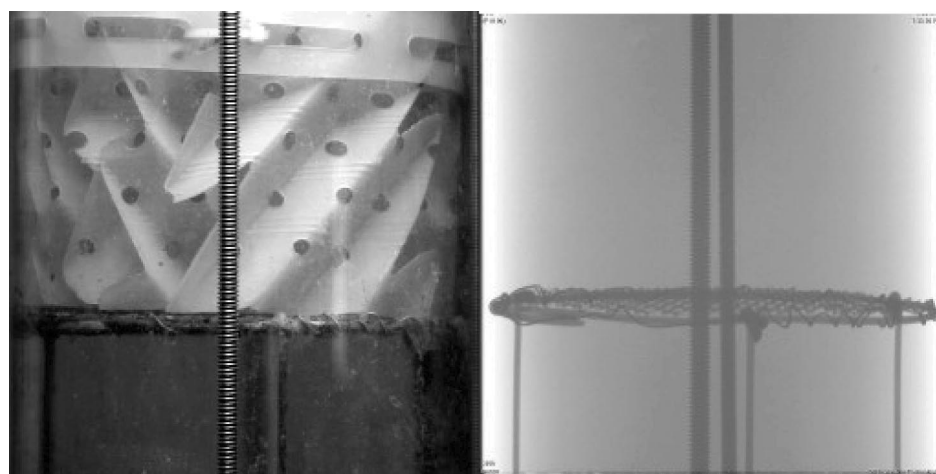


**Figure 1.** Photograph (left) and radiograph (right) both show the lowest element of packing.

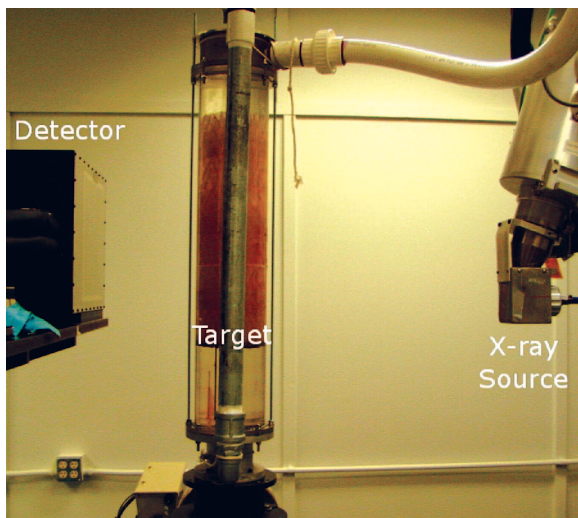


**Figure 2.** Contacting column mounted between an X-ray source (right) and cardiac detector (left).

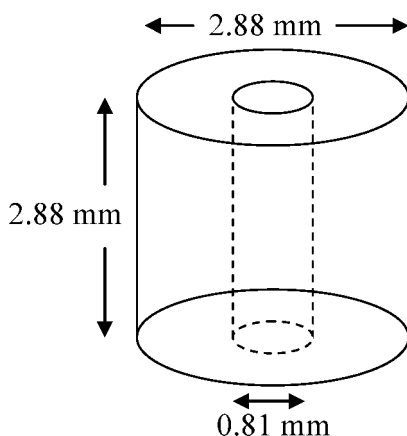


**Figure 3.** Schematic particle drawing.

fact that the attenuation coefficient is a strong function of X-ray energy, the complete solution would require solving the equation over the range of the effective X-ray spectrum:

$$I = \int I_0(E) \exp\left[\sum_i (-\mu_i(E)x_i)\right] dE \quad (1.3)$$

However, such a calculation is usually not done in industrial X-ray scanning as the precise shape of the X-ray profile, and

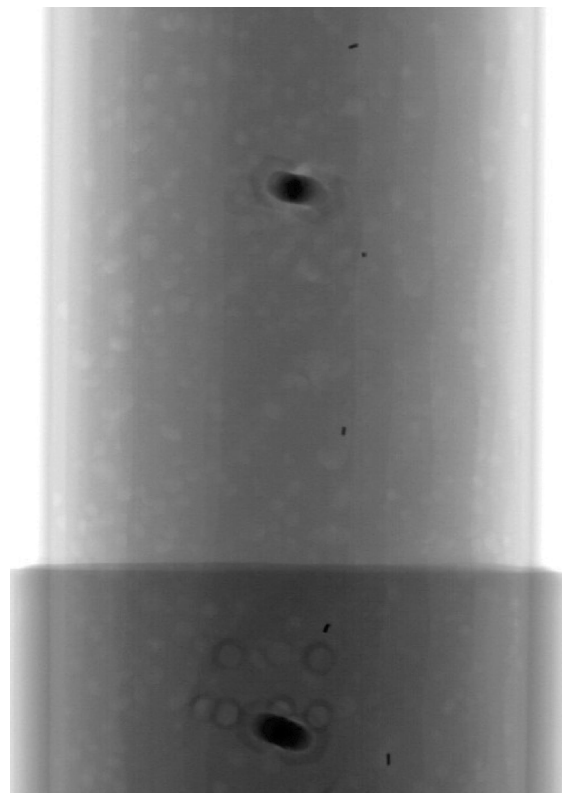


**Figure 4.** Radiograph to assess particle visibility. Solder length (mm) from top to bottom: 2, 1, 1.5, 2.1, and 2.3.

its variation at off-center angles in a fan or cone beam is usually only estimated theoretically rather than measured.<sup>11</sup>

Attenuation is dependent on both material and beam energy. At low energies, the attenuation is proportional to the material's atomic number raised to a power. This relationship becomes linear at higher energies.<sup>11</sup> This can be problematic when polyenergetic sources are used. As the beam passes through an object, the lower energy X-rays are preferentially attenuated, resulting in a beam with a higher average energy than the initial beam. This can result in artifacts during some X-ray imaging. Artifacts are features in the image that are not present in the scanned object. This phenomenon is known as beam hardening and is especially apparent when using low-energy sources or scanning long lengths and/or very dense material. Beam hardening can be mitigated by placing a dense material after

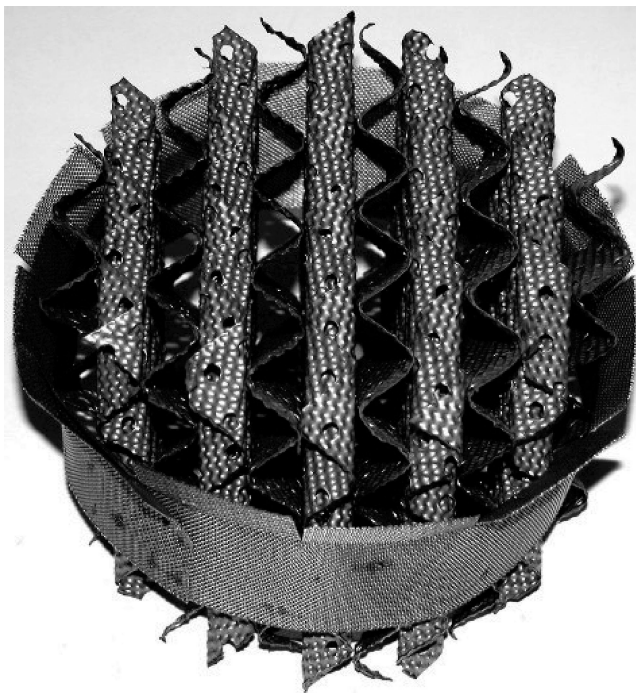


**Figure 5.** Picture of the structured packing Mellapak 250 Y in stainless steel.

the X-ray source (prefiltering) or prior to the detector (postfiltering) to remove low-energy X-rays.

**1.3. X-ray Radiography Equipment.** An X-ray scanner consists of an X-ray source(s) and detector(s) arranged on opposite sides of the object to be scanned. Industrial systems commonly employ isotope decay, X-ray tubes, or linear accelerators as sources. Isotope sources produce X-ray beams of one or two energy levels; however, the flux is much lower than that of tube sources or linear accelerators.<sup>12</sup> Linear accelerators and tube sources both produce polyenergetic beams, with linear accelerators being capable of producing greater energy than tube sources.<sup>12</sup> The higher energy output of linear accelerators lends them to industrial usages where large or very dense material must be scanned.

Industrial detectors are classified as scintillation or ionization detectors. Ionization detectors typically use a noble gas, which produces a measurable current when irradiated with X-rays. Scintillation detectors use a material that fluoresces under irradiation.<sup>12</sup> The visible light is read by an optical enhancement device, such as photomultiplier tubes or photodiodes, which convert the light to an electrical signal. Traditionally, these detectors are arranged either in a line or rectangular pattern for use with fan or cone beam scanners, respectively. The most recent advancement in X-ray detector technology is the flat panel detector. Flat panel detectors build on the traditional scintillation detectors by adding a layer of amorphous silicon beyond the photodiodes. This layer of silicon has been imprinted with millions of microscopic transistors that are connected to the photodiodes. The layer of silicon is known as a thin-film-transistor (TFT). Each photon striking the photodiodes is converted into an electron–hole pair. The variation in intensity across the TFT creates an electrical pattern, which can quickly be read and saved in a digital state.

The use of microscopic transistors allows the detector spacing to approach that of a continuous detector, giving much finer spatial resolution. The use of the TFT circuitry also allows the voltage variation to be read quickly and stored in a digital form

as opposed to traditional detectors, which require the analog voltage of each individual detector be read and stored. In this way, a macroscopic height can be scanned quickly with a high spatial resolution.

**1.4. Radiographs.** A radiograph is a gray-scale contour plot of X-ray intensity at each point along the detector. The data range is determined by the bit depth of the detector with a 16 bit detector capable of reporting 65 536 distinct intensities. Prior to scanning, a blank radiograph is taken without the object mounted between the source and detector. The X-ray intensity measured during this scan is at a maximum and is a function of air temperature, humidity, and barometric pressure. The source power is adjusted so that the detector is saturated during the blank scan. This provides maximum contrast in the proceeding scans. A picture and radiograph of the lowest packing element are shown in Figure 1.

**1.5. X-ray Particle Tracking Velocimetry (XPTV).** Particle tracking velocimetry (PTV) is an established technique for experimental observation of flow field physics. PTV hinges on the observation of particles, which behave in the same manner as the phase of interest. Traditionally, particle tracking has depended on optical access to track reflective or fluorescing particles. This shortcoming has prevented its application to multiphase flows, optically opaque fluids, and complex equipment that cannot be modified for optical access. However, recent advances in nonoptical imaging, such as those based on X-rays, have enabled researchers to extend PTV to characterize previously inaccessible flows.

Most recently, X-ray-based particle tracking velocimetry (XPTV) has been employed to study flow phenomena within two and three phased bubble columns.<sup>13–17</sup> Seeger et al. first employed XPTV to study 2D flow in a water-filled bubble column with low void fraction as a benchmark against optical methods.<sup>16</sup> This method was then extended to three dimensions with the use of a second X-ray source and detector. Four-hundred sixty-five image pairs were taken over a 19 s span in a glycerin-filled bubble column operating at a 10.5% void fraction.<sup>16</sup> The use of glycerin as a continuous phase was necessary to slow the particle velocities and facilitate image analysis and particle tracking. Seeger et al. extended this method to observe fluid dispersion and measure solid dispersion and solid-phase velocities in a three-phase bubble column by matching the X-ray attenuating particles to the density and size of the solid phase.<sup>15,17</sup>

## 2. Experimental Equipment

**2.1. X-ray Equipment.** Scans were performed at General Electric's (GE) Quality Technology Center (QTC) in Cincinnati, OH. The system consists of a linear accelerator X-ray source capable of a 220 kV potential paired with a flat panel, cardiac detector. The detector was amorphous silicon, structured cesium iodide with a 200  $\mu\text{m}$  pixel pitch and was capable of 30 Hz recording of 16 bit data. This system was selected due to the high temporal and spatial resolutions of the cardiac detector.

This system, shown in Figure 2, generates a conical X-ray beam, which is read by a flat panel detector measuring approximately 14 cm high by 15 cm wide. This scanner utilizes a positioning table, which can manipulate the object in the  $x$ ,  $y$ ,  $z$ , and  $\theta$  directions. The source was operated at 200 kV and 1.6 mA, which saturated the detector during blank scans.

**2.2. Particles.** A method similar to that of Kertzscher et al. was used to create neutrally buoyant, X-ray absorbing particles.<sup>14</sup> High-density polyurethane foam was machined into cylinders 2.88 mm in diameter and 2.88 mm tall. A cylindrical,

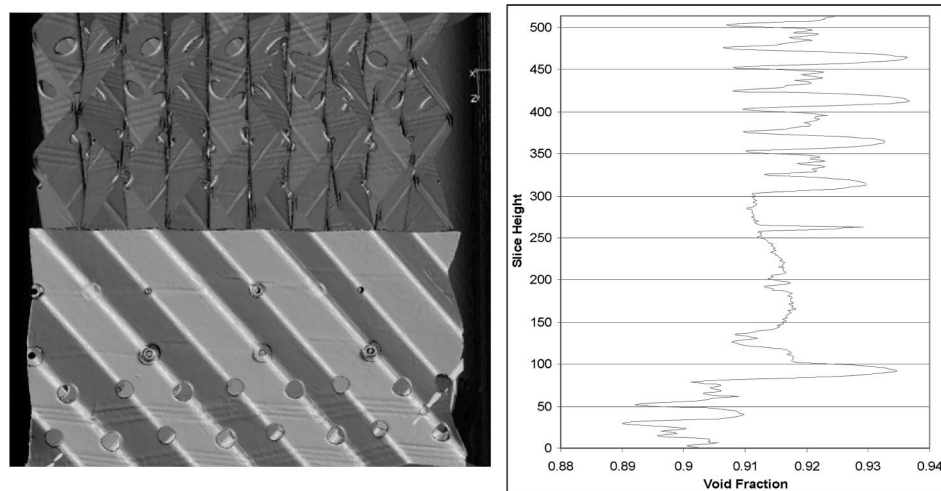


**Figure 6.** Bisected CT reconstruction of the packing joint (left) and the void fraction of each slice (right).

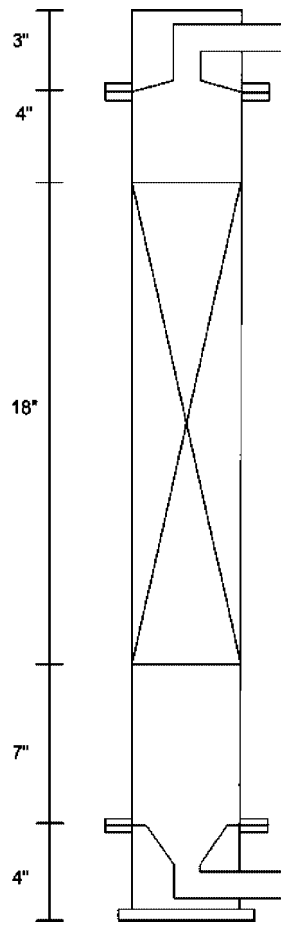


**Figure 7.** Schematic of the column.

coaxial cavity 0.81 mm in diameter was then bored through the foam as shown in Figure 3. This cavity was filled with a lead alloy to make the particles strongly absorb X-rays.

Solder was selected as the X-ray absorbing material due to its high lead content (~40%) and wide availability as a wire with many different diameters. Prior to committing to solder, a test was conducted to assess its visibility under scan conditions. Several pieces of 0.56 mm [0.022 in.] diameter solder with lengths from 1 to 2.3 mm [0.0394 to 0.0906 in.] were taped to the center of a section of plastic packing. The packing was placed in a 10.2 cm [4 in.] ID PVC pipe, which was sealed on one end and filled with water. The apparatus was then scanned

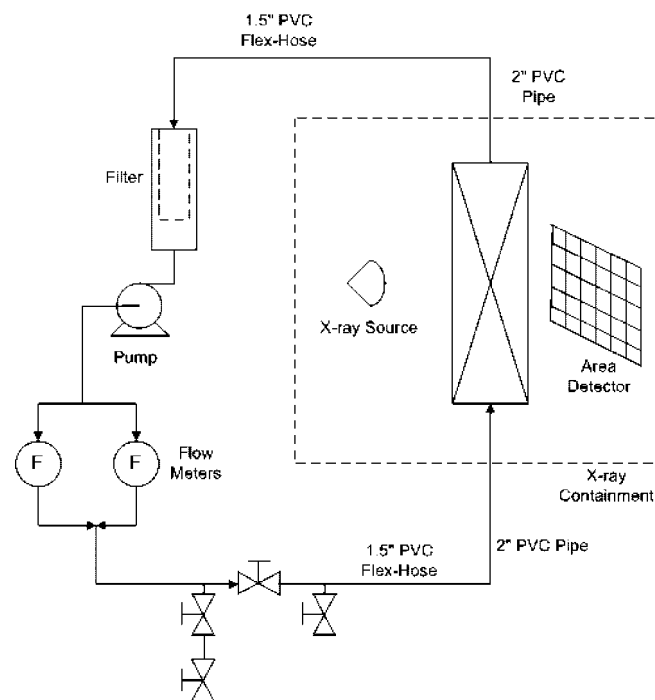


**Figure 8.** Process flow sheet.

**Table 1.** Similarity Theory Calculation of Flow Rates in a 14.6 cm [5.75 in.] ID Column from F-factor

$F_s$	Air		H <sub>2</sub> O			$N_{Re}$
	(m/s [ $\text{kg}/\text{m}^3$ ] <sup>1/2</sup> )	(ft/s [ $\text{lb}/\text{ft}^3$ ] <sup>1/2</sup> )	m/s	ft/s	$\text{m}^3/\text{hr}$	
1.83		1.5	0.111	0.366	6.7	29.6
1.95		1.6	0.119	0.390	7.2	31.6
2.07		1.7	0.126	0.414	7.6	33.6
2.20		1.8	0.134	0.439	8.1	35.5
2.32		1.9	0.141	0.463	8.5	37.5
2.44		2.0	0.149	0.488	9.0	39.5
						21 703

at the University of Texas Computed Tomography (UTCT) facility with source and detector settings mirroring those that would be used at GE. The results are shown in Figure 4.

This experiment utilized a solder 0.56 mm in diameter and composed of tin (62%), lead (36%), and silver (2%). Knowledge of the foam density and volume, along with the solder diameter and an approximation of its density, allowed for the calculation

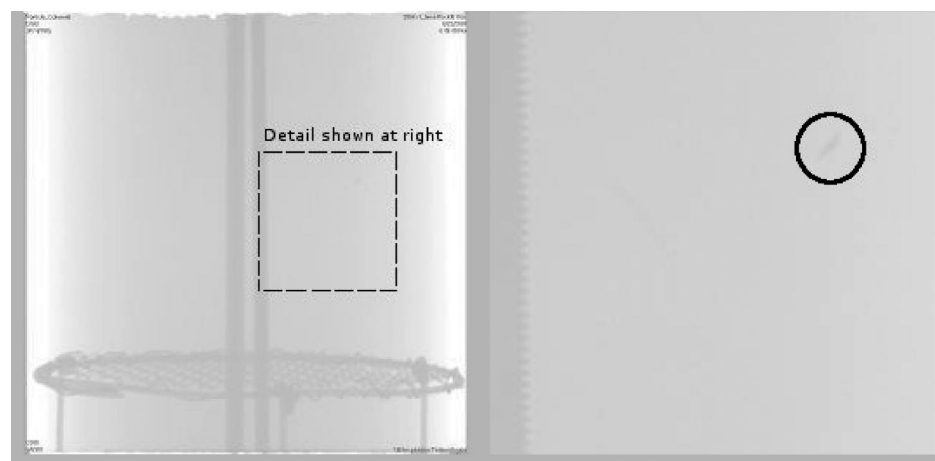


**Figure 9.** Frame 74 excerpted from the video of the fifth experimental run (left) and a detail showing the particle in the frame (right).

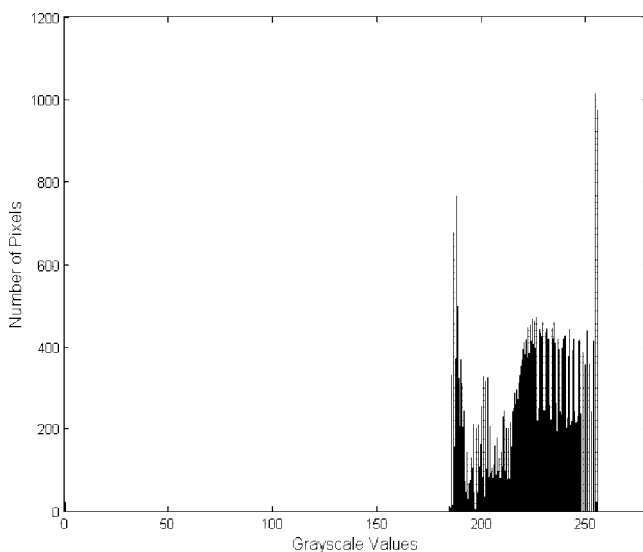


**Figure 10.** Histogram of frame 74 from video of fifth experimental run.

of the solder length that would yield a neutrally buoyant particle. This length was cut from the wire and secured inside the foam with super glue. The particles were tested in water and adjusted as needed to yield neutral buoyancy.

**2.3. Packing.** Structured packing is a high surface area separation column internal with relatively low pressure drop. It is comprised of vertical, corrugated sheets either bound or pinned together (Figure 5). The angle of corrugation, surface treatments, specific surface area, and perforations vary by manufacturer and model. Each packing element is 25 to 30 cm [10 to 12 in.] high with successive elements rotated 90° about the column axis to ensure liquid redistribution. Structured packing is commonly made of stainless steel, plastic, or ceramic.

A plastic packing was used to limit the absorption of X-rays and increase the visibility of the lead-containing particles. Specifically, plastic Mellapak 250Y was supplied by Sulzer ChemTech. This packing has a specific area of 250 m<sup>2</sup>/m<sup>3</sup> and corrugated channels, which are at a 45° angle from the horizontal. The method of Green et al. was employed to determine the packing void fraction via X-ray CT.<sup>12</sup> CT scans were performed at the UTCT facility on a 15.4 cm height of packing centered on a joint. The scans were analyzed to yield the void fraction of each slice (Figure 6). The average void fraction was found to be 91.6%. Three half-elements, each approximately 15.2 cm [6 in.] tall, were used in this experiment.

**2.4. Column.** The column was constructed from three pieces: a cylindrical aluminum base, a hollow polycarbonate tube that housed the packing, and a machined polycarbonate cap. The tube and cap each have flanges to connect them to the adjacent column sections. The flanges at the bottom of the tube and cap are designed to hold an O-ring, which ensures a watertight seal. A threaded rod was secured to the aluminum base and a steel plate above the cap to provide a compressive force.

A hole was drilled in the side of the base and tapped to accept threaded piping 3.08 cm [1 in. NPT] in outside diameter (OD). The water enters the column through this opening. This opening proceeds to the central axis of the column and turns 90° upward (Figure 7). The opening is conical from here to the top of the 10.2 cm [4 in.] tall base. The polycarbonate tube is 71.12 cm [28 in.] tall with an outer diameter of 15.24 cm [6 in.] and a 0.3175 cm [0.125 in.] wall thickness. The packed section begins 17.78 cm [7 in.] above the base and is 45.72 cm [18 in.] tall. The cap was fashioned out of a solid polycarbonate cylinder 15.24 cm [6 in.] in diameter. A 15° cone was machined onto the underside of the cap. This acts to funnel the flow to the center of the cap where it enters a 2.54 cm [1 in.] hole. This hole turns 90° and exits out the side of the cap (Figure 7). The exit is drilled and tapped to accept threaded piping 3.08 cm [1 in. NPT] in outside diameter.

**2.5. Instrumentation.** The liquid flow rate was measured via two MicroMotion F50 flow meters. The process flow was split and flowed through the flow meters in parallel (Figure 8) to reduce pressure drop in the system as well as allow measurement of flows greater than the 7.95 m<sup>3</sup>/hr [35 gpm] upper limit of each flow meter. The flow meters output a 4–20 mA signal. This signal was converted to a 1–5 V signal via a 250 Ω ± 0.01% resistor and read into the National Instruments (NI) LabView software with an NI USB-6008 data acquisition card. A LabView program was prepared to convert the voltage signal to flow units, and sum the individual flow rates, as well monitor and log the data to a file.

**2.6. Piping.** Pressure drop had to be minimized to reach water flow rates that would simulate the vapor-phase Reynolds numbers commonly encountered in vapor–liquid contactors. For this reason, the majority of the piping was rigid 5.08 cm [2 in.] schedule 40 pipe. This was supplemented with 3.81 cm [1.5 in.] schedule 40 flexible PVC piping wherever connections were made to process equipment and where the piping crossed the X-ray containment.

Because damage would result if the particles were to flow through the pump or flow meters, the particles were introduced

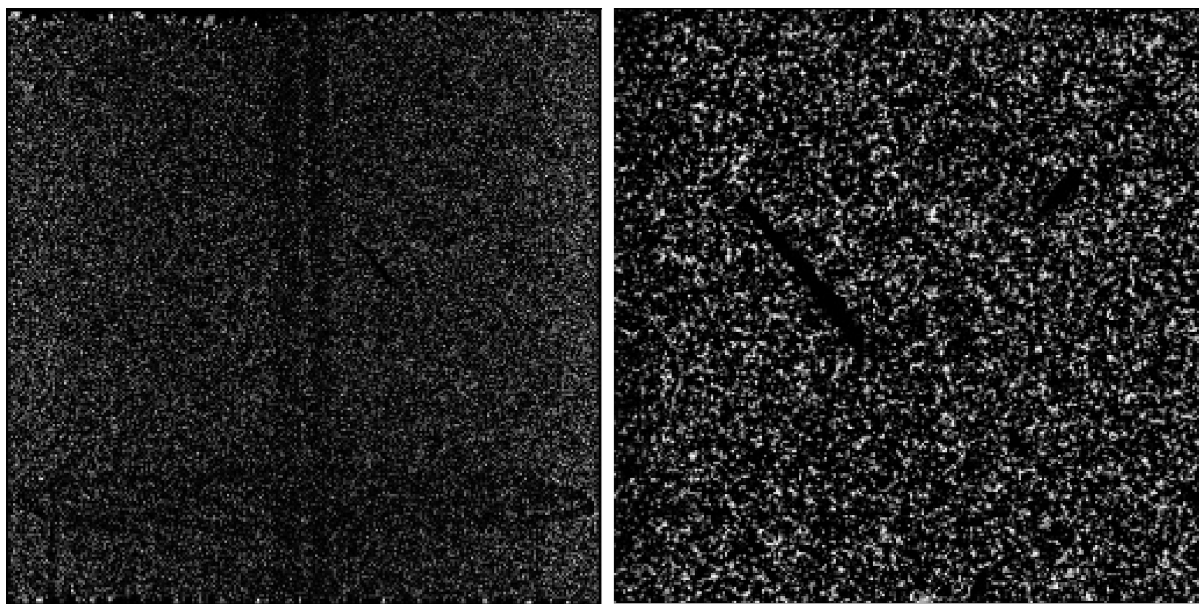


**Figure 11.** Frame 74 from the video of the fifth experimental run after frame differencing (left) and an excerpt highlighting particles (right).

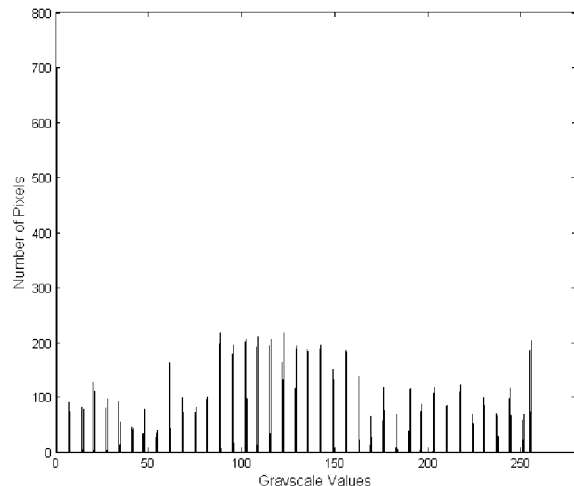


**Figure 12.** Histogram of frame 74 from the video of experiment 5 after being differenced with the first frame.

after the flow meters and removed prior to the pump. A short pipe with valves at each end was connected to a T (Figure 8) in the process piping. This was used as an air lock to facilitate introducing the particles to the system under flow conditions.

An 800  $\mu\text{m}$  filter bag was used to prevent the particles from entering the suction of the pump. The filter had valves attached

**Table 2. X Filtering Element**

1	0	1
0	1	0
1	0	1

**Table 3. Cross Filtering Element**

0	1	0
1	1	1
0	1	0

both upstream and downstream, which allowed particles to be removed without allowing air to enter the process or losing water from the system.

### 3. Experimental Method

**3.1. Flow Rates.** This research sought to document the physics occurring in the vapor phase of a vapor–liquid contactor. However, it was necessary to use water as the process medium to allow for the creation of neutrally buoyant particles. Therefore, similarity theory was employed to choose water flow rates that would exhibit behavior analogous to that seen in the vapor phase of industrial contactors.

Flow rates in industrial vapor–liquid contactors are traditionally quantified in terms of an F-factor (units of velocity times the square root of density, denoted as  $F_S$ ) and typical operating rates are from 1.8 to 2.5 m/s \*  $(\text{kg}/\text{m}^3)^{0.5}$  [1.5 to 2 ft/s \*

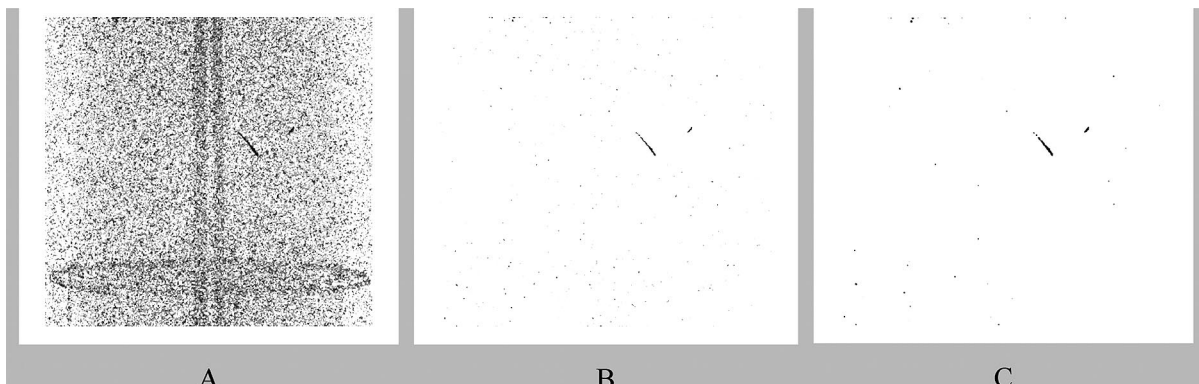


**Figure 13.** Figures showing the results of successively applying a max (A), Gaussian (B), and minimum (C) image filtering.

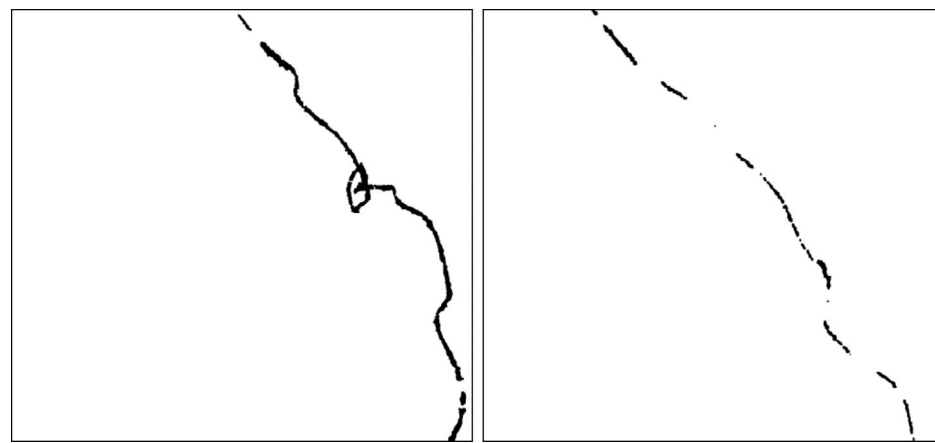


**Figure 14.** Composited images showing the full path of two particles observed in experiment 5.

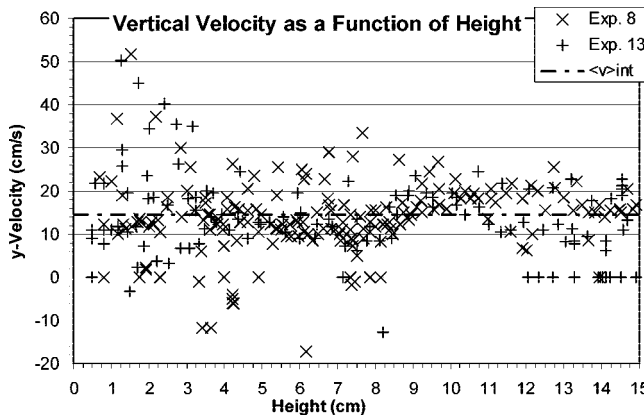


**Figure 15.** Vertical velocities measured at  $7.95 \text{ m}^3/\text{hr}$  [35 gpm] through the lower joint plotted as a function of their height in the image.

( $\text{Lb}_m/\text{ft}^3$ ) $^{0.5}$ ]. Using the definitions of the F-factor and Reynolds number, one can set the water and air Reynolds numbers equal and solve for water velocity in terms of the corresponding vapor F-factor. This calculation is tabulated in Table 1. Data was taken in this study at flow rates of 4.54, 5.68, 6.81, and  $7.95 \text{ m}^3/\text{hr}$  [20, 25, 30, and 35 gpm].

**3.2. Particle Introduction/Recovery.** The particles were introduced through a T in the process piping immediately after the flow meters. A 15.24 cm [6 in.] piece of Tygon tubing with valves on either end was connected to this T (Figure 8). To

introduce particles at steady state, both valves were left closed while the system was brought to a steady flow rate. Then the outer valve was opened and particles were placed in the tubing. Next, the outer valve was closed and then the inner valve was opened and the particles allowed to enter the process stream.

The particles were introduced in batches of 5–10 particles at a time. This increased the odds of seeing and recording particles in each experimental run. After each experimental run, the pump was shut off and the filter isolated from the process. The filter could then be opened and the particles recovered.

**3.3. Movie Acquisition.** The X-ray scanner recorded movies on the computer system used to monitor and control the scanner. This computer system displayed radiographs in real time and read radiographs into its buffer at a 30 Hz sampling rate. At this rate, the buffer could accommodate 3 s of radiographs. Movies in DICOM format were created by dumping the buffer to the hard drive.

#### 4. Data Analysis

Videos were recorded at 30 Hz for approximately three seconds and written in grayscale DICOM format. As can be seen in Figure 9, the particles show limited contrast with the background. The poor contrast is likely a product of two factors.

The facility used for this experiment primarily performs computed tomography (CT) scans. As described above, beam hardening is a major concern when performing CT scans. For this reason,

**Table 4.** Velocity Calculations Performed for the Fifth Experiment

frames	Positions (px)				Component Velocity (cm/s)					
	Initial		Final		Displacement (cm)		$\text{H}_2\text{O}$		Air (Equivalent)	
	x	y	x	y	x	y	x	y	x	y
60	986	857	971	809	-0.227	0.726	-6.8	21.8	-102	326
61	966	813	942	713	-0.363	1.512	-10.9	45.4	-163	679
62	935	712	950	571	0.227	2.132	6.8	64.0	102	958
63	953	603	905	493	-0.726	1.663	-21.8	49.9	-326	747
64	912	503	846	449	-0.998	0.816	-29.9	24.5	-448	367
65	847	459	831	429	-0.242	0.454	-7.3	13.6	-109	204
66	842	438	797	432	-0.680	0.091	-20.4	2.7	-306	41
67	802	440	758	449	-0.665	-0.136	-20.0	-4.1	-299	-61
68	758	450	774	419	0.242	0.469	7.3	14.1	109	211
69	774	432	786	406	0.181	0.393	5.4	11.8	82	177
70	783	424	773	385	-0.151	0.590	-4.5	17.7	-68	265
71–73			Stationary				0.0	0.0	0	0
74	776	382	752	407	-0.363	-0.378	-10.9	-11.3	-163	-170
75	773	390	747	427	-0.393	-0.559	-11.8	-16.8	-177	-251
76	750	422	747	458	-0.045	-0.544	-1.4	-16.3	-20	-245
77	749	451	754	484	0.076	-0.499	2.3	-15.0	34	-224
78–84			Stationary				0.0	0.0	0	0

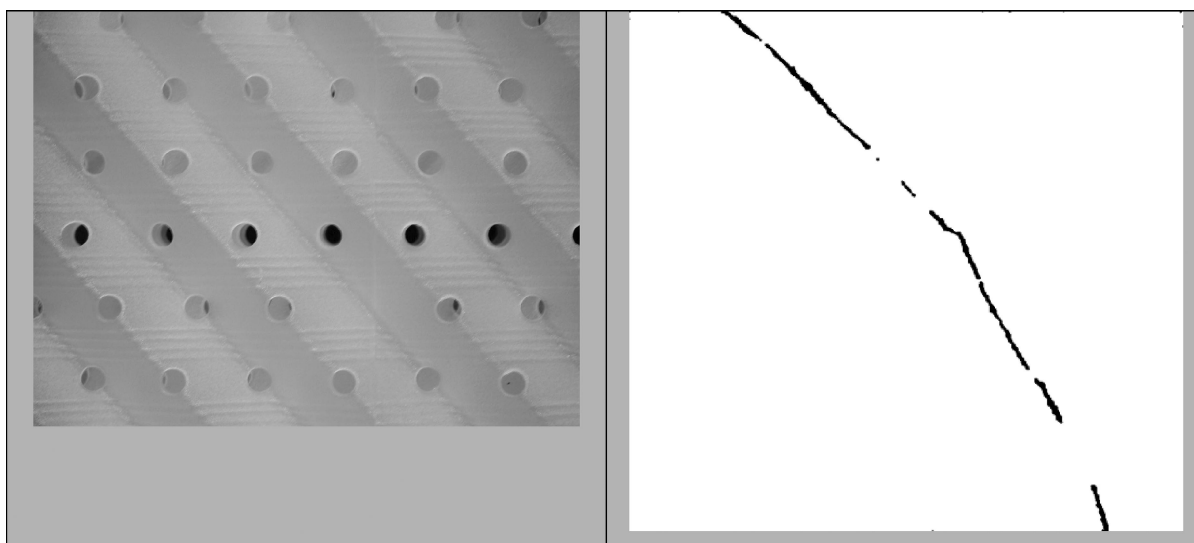


**Figure 16.** Particle from the fifth experiment (1st packing element,  $5.68 \text{ m}^3/\text{hr}$  [25 gpm]) showing a predominately linear path.

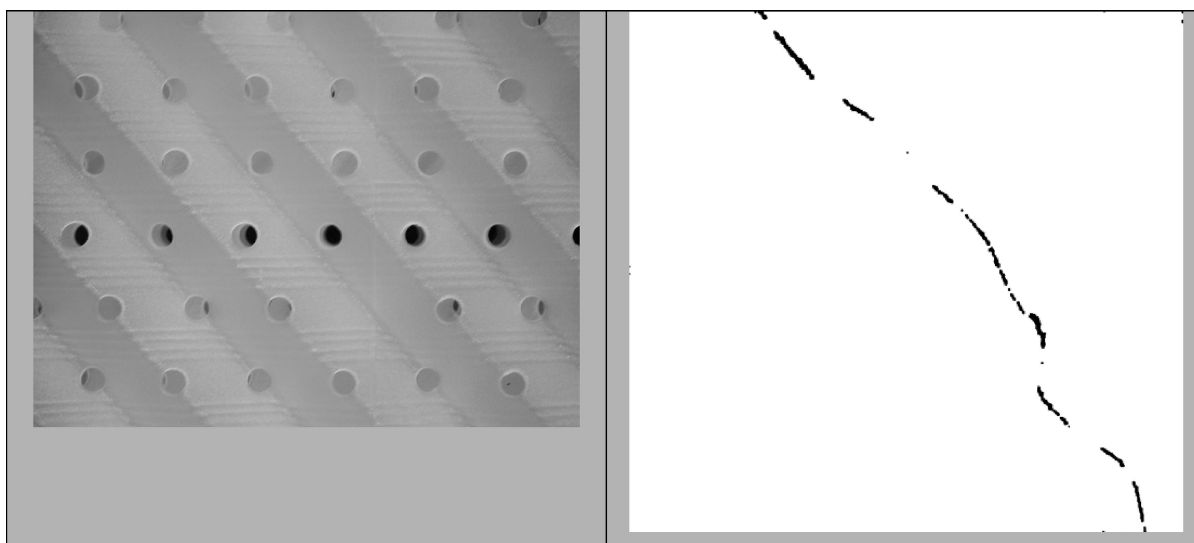


**Figure 17.** Trajectory recorded in the fifth experiment (1st packing element,  $5.68 \text{ m}^3/\text{hr}$  [25 gpm]) shows minor flow disruptions at the packing interface.

the X-ray beam at this site is prefiltered to remove low-energy X-rays. Because variation in X-ray attenuation between materials is less significant at higher beam energies, the detector measured a smaller difference in the transmission of water alone (background) versus water with a particle. This resulted in a compressed histogram in (Figure 10). A compressed histogram is one in which the data take up only a small amount of the available range. An unfiltered, lower-energy X-ray beam would have given better contrast, provided it could penetrate the target.

The second problem arises from the high velocities studied in this experiment. This research documents superficial velocities of 7.53, 9.42, 11.3, and 13.4 cm/s [2.97, 3.71, 4.45, and 5.19 in./s]. If it is assumed that each frame captures  $\frac{1}{30}$  of a second, the particles would travel 2.51, 3.14, 3.77, and 4.39 mm [0.0988, 0.124, 0.148 and 0.173 in.] in each frame, respectively. At all but the lowest flow rate, the particles travel a distance that is greater than the particle dimensions. This means that the particle attenuates the beam at each pixel for only a fraction of the exposure time and the pixel receives the full background intensity for the remainder. Because the detector records the total intensity during the exposure, this time averaged exposure leads to decreased contrast between the background and the particles.

The DICOM formatting of the source data might also have contributed to a compressed histogram. Data ranging and thresh holding were performed automatically during the recording process according to the DICOM standard. If the raw data formats were available, a more guided approach to data conversion and manipulation could yield better contrast.

To correct for the compressed histogram, the DICOM video files were read into *Matlab* where each frame was converted to an 8 bit TIFF image. The TIFF file format represented each pixel as a gray level between 0 (black) and 255 (white). This allowed the data to be manipulated mathematically to increase the available contrast.

Temporal persistence, or frame differencing, was used to remove static and de-emphasize nearly static elements.<sup>18,19</sup> This method consisted of setting the first frame in each video as a reference and performing a point-by-point subtraction of all subsequent frames. Any pixels which do not change would go to zero and any pixels that change only due to noise would become very small in magnitude. By contrast, any pixel containing a particle would result in background values of the reference ( $\sim 255$ ) being subtracting from pixel values ( $\ll 255$ ) and retain a large magnitude. To maximize the resulting data,

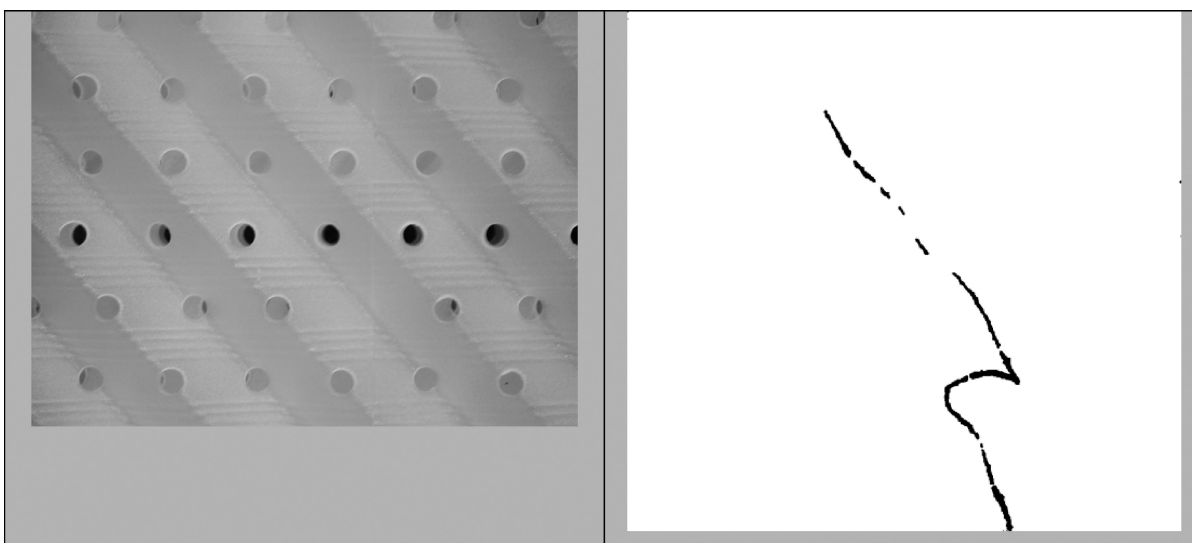


**Figure 18.** Some particles showed flow disturbance upon entering the packing. Flow through lowest packing element at  $5.68 \text{ m}^3/\text{hr}$  [25 gpm].



**Figure 19.** Channels in adjacent packing sheets intersect at  $90^\circ$  angles.

a full-scale contrast stretch was performed to fit the data to the available range and the image inverted so that the particles appear black on a white background.<sup>18,19</sup> Figure 11 shows that the frame differencing and contrast stretch not only made the particle appear clearer but also reveal particles not visible in the original data. This is likely due to the increased utilization of the available data range (Figure 12).

Morphological filtering was used to reduce background noise based on feature size.<sup>18,19</sup> Morphological filters use a structuring element, or window, to select a subset of pixels corresponding to window geometry. The pixel values are sampled according to a Boolean operation and the results are used to generate a new image which retains only prominent features from the original image. Part A of Figure 13 shows the results of applying a successive maximum operations with an X element (Table 2) and then a cross

element (Table 3). This was followed by a  $3 \times 3$  Gaussian filter (part B of Figure 13) and a minimum operation with the X and cross elements (part C of Figure 13).

Composite images were created to highlight qualitative flow phenomena. To create composites, the individual frames were inverted so that the particles were white (255) and the background black (0). The frames showing a particle's path were then summed by matrix addition to yield the composite image. This is shown for two particles in Figure 14.

## 5. Results and Discussion

Thirteen experiments were videotaped. These experiments were conducted at flow rates ranging from  $4.54$  to  $7.95 \text{ m}^3/\text{hr}$  [20 and 35 gpm]. Videos were taken of flow through three regions: the first (lowest) packing element, the joint between

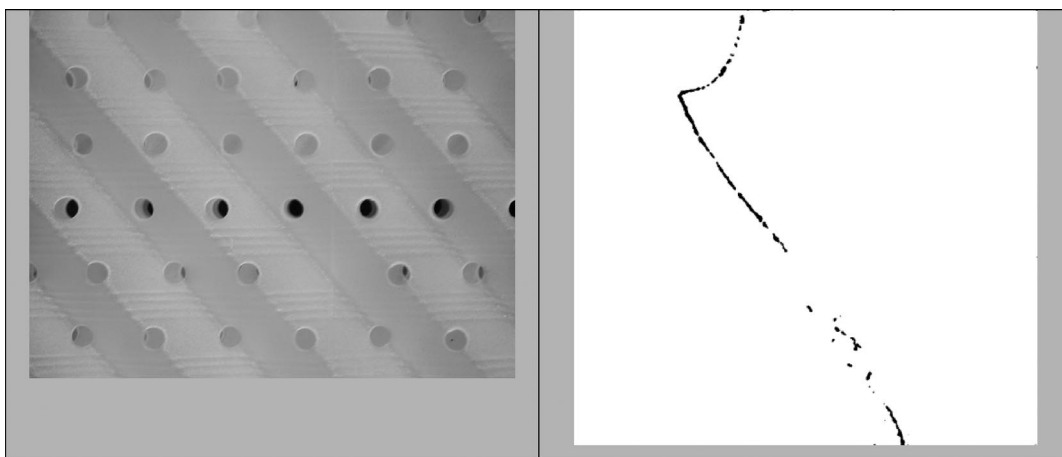


**Figure 20.** Particle path from the seventh experiment (1st packing element,  $5.68 \text{ m}^3/\text{hr}$  [25 gpm]) shows a particle transition between adjacent channels in the packing.

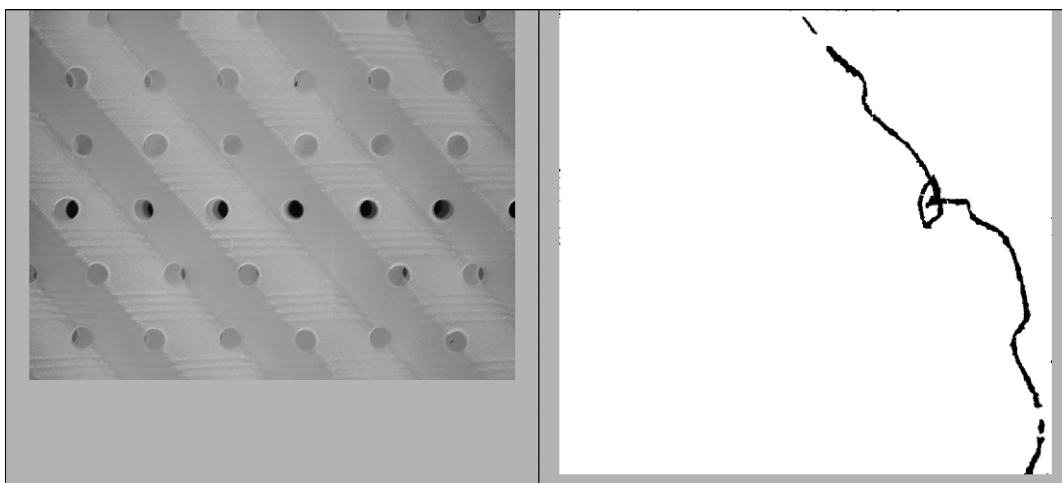


**Figure 21.** Initial vertical trajectory likely indicates wall flow prior to an obstruction, which forces the particle into the packing. Flow at  $5.68 \text{ m}^3/\text{hr}$  [25 gpm] through the 1st packing element.

the first and second packing elements, and the second (middle) packing element. Flow within packing elements largely followed linear paths, whereas flow at the joints and wall exhibited chaotic flow with recirculation zones and discontinuous velocities.

Features of known length within the radiographs were used to create a conversion between image and real world dimensions. This, combined with the assumption that the 30 Hz frame rate equaled a  $1/30$  of a second exposure, enabled the calculation of instantaneous velocities using the initial and final positions of the particles in each radiograph. Two experiments recorded velocities through the lower joint under a  $7.95 \text{ m}^3/\text{hr}$  [35 gpm] volumetric flow rate. Figure 15 graphs all velocities recorded in these experiments as a function of height. On average, the particle velocities closely approximate the calculated interstitial velocity of  $14.4 \text{ cm/s}$  [5.67 in/s]. This suggests that the physics and velocities captured are representative of the bulk flow.

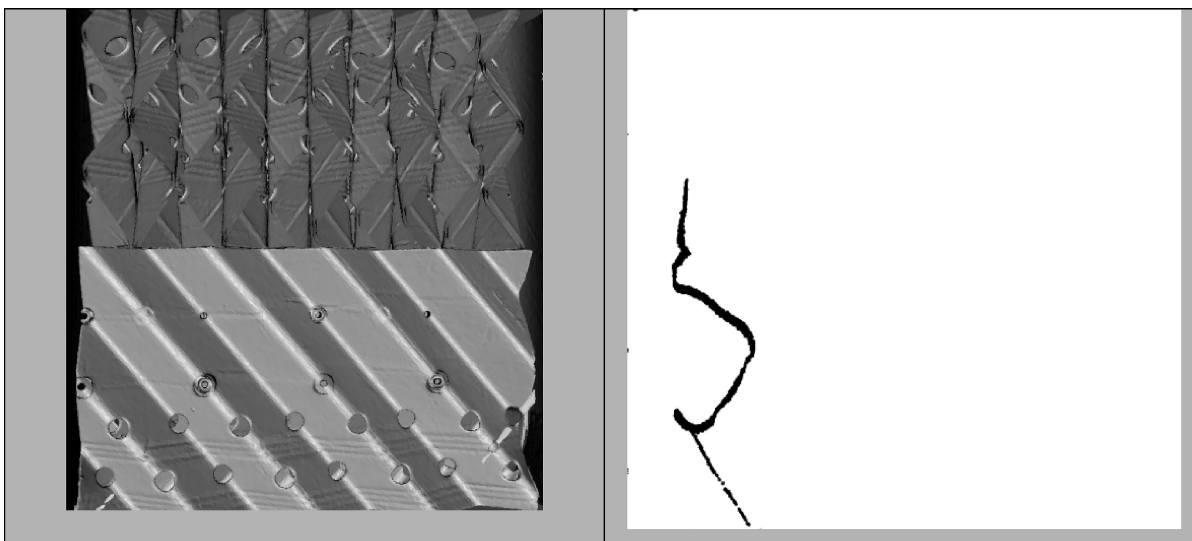
Table 4 shows an excerpt of velocity calculations performed on data taken from the fifth experiment. The displacement per frame is calculated directly from the first and last positions occupied by the particle. The instantaneous velocity of the experimental fluid can be calculated by multiplying the frame displacement by the frame rate employed. Because locations within the image are indexed by horizontal and vertical positions, component velocities are obtained directly. This is ideal for comparison with CFD predictions as many CFD software packages report local velocities in component notation

and allow the user to specify custom coordinate systems to further simplify matching the predicted and measured velocities. Table 4 also shows the equivalent air velocity calculated using similarity theory.

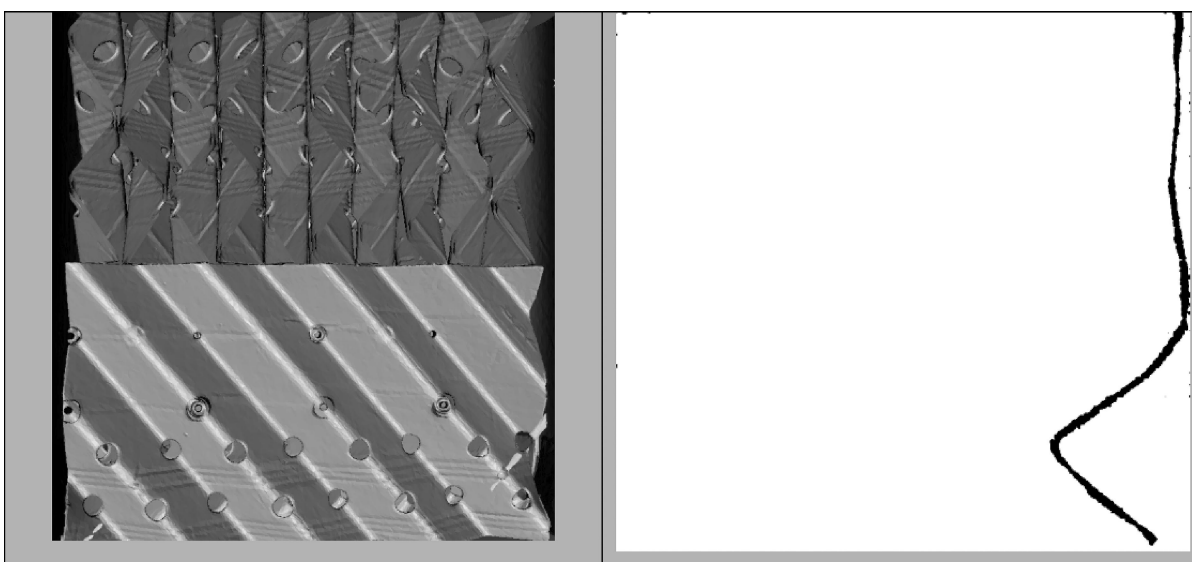
Figures 16, 17, 18, 19, and 20 show particle paths through the lowest packing element recorded during experiments with flow rates of  $5.68 \text{ m}^3/\text{hr}$  [25 gpm]. In each figure, the particles show a tendency to flow smoothly at an angle that corresponds to the corrugation angle of the packing ( $45^\circ$ ). Figure 17 shows the particle curve upward as it enters the packing and follow an increasingly linear path through the packing. This suggests the channels enforce a uniform and linear flow pattern within the packing.

Figure 18 shows a much greater flow disturbance upon entering the packing. The magnitude of the lateral displacement suggests the particle leaves the original channel and flows horizontally through a channel in the adjacent packing sheet (Figure 19). This is followed by a sharp change in direction as the particle seems to enter and flow with a channel in the original packing sheet. Both the horizontal travel and the discontinuous change in velocity would result in high energy dissipation and pressure drop.

Figure 20 depicts a particle path recorded during the seventh experiment. In this path, the particle appears to make a quick transition between channels in adjacent packing sheets. This region is likely characterized by high shear and turbulence. In



**Figure 22.** Composite of experiment 8 shows a smooth transition between adjacent channels and a smooth transition through the packing joint. Flow through the packing joint at  $5.68 \text{ m}^3/\text{hr}$  [25 gpm].



**Figure 23.** Video of experiment 8 shows a particle leave the lower packing element and entering a region of wall flow. Flow through the packing joint at  $5.68 \text{ m}^3/\text{hr}$  [25 gpm].

spite of this, the flow does not exhibit large recirculation. This, coupled with the abrupt horizontal to vertical transition in Figure 18, suggests transitions between adjacent channels do not exhibit wide scale flow disruption.

Figure 21 shows a path that suggests there is a large scale recirculation zone in the middle of the packing. However, the first half of the path shows predominately vertical travel. This likely shows a particle flowing along the wall before encountering an obstruction, such as the wiper band. This obstruction seems to create a separation point, which results in a recirculation zone. As the particle exits this zone, it enters the packing and flows smoothly through it.

Figure 22 shows the path of a particle as it transitions from the lowest to middle packing elements under a  $5.68 \text{ m}^3/\text{hr}$  [25 gpm] flow rate. Interestingly, this path shows two transitions between packing channels in the lowest packing element with the first transition exhibiting slight negative flow and the second seemingly smooth. The particle exhibits uniform and smooth flow as it leaves the first packing element and enters the second.

Performance at the joint suffered from poor flow integration as well as recirculation and stagnant zones. Figure 23 shows a

particle that is shunted toward the wall by the channels in the lower packing. The particle leaves the lower packing element at the joint but does not enter the next packing element. Instead, the particle flows along the wall and entirely bypasses the packing element. This behavior would result in reduced contacting and limited mass transfer in industrial applications.

Negative flow was a common observation at the joint (Figure 24). The particle would enter the second packing element and then reverse direction. Most often the particle would begin flowing up the column again after some horizontal travel. This behavior is suggestive of a nonuniform pressure profile at the entrance to the second packing element and, presumably, all subsequent packing elements. This phenomenon could result in channeling and poor distribution.

Figure 25 shows a transition between packing elements. Most notable is the large-scale recirculation and corresponding negative flow. This is indicative of separation points forming at the end of the packing sheets. The recirculation would be a significant source of pressure drop and poor contacting performance. Also worth noting is the smooth and uniform nature of

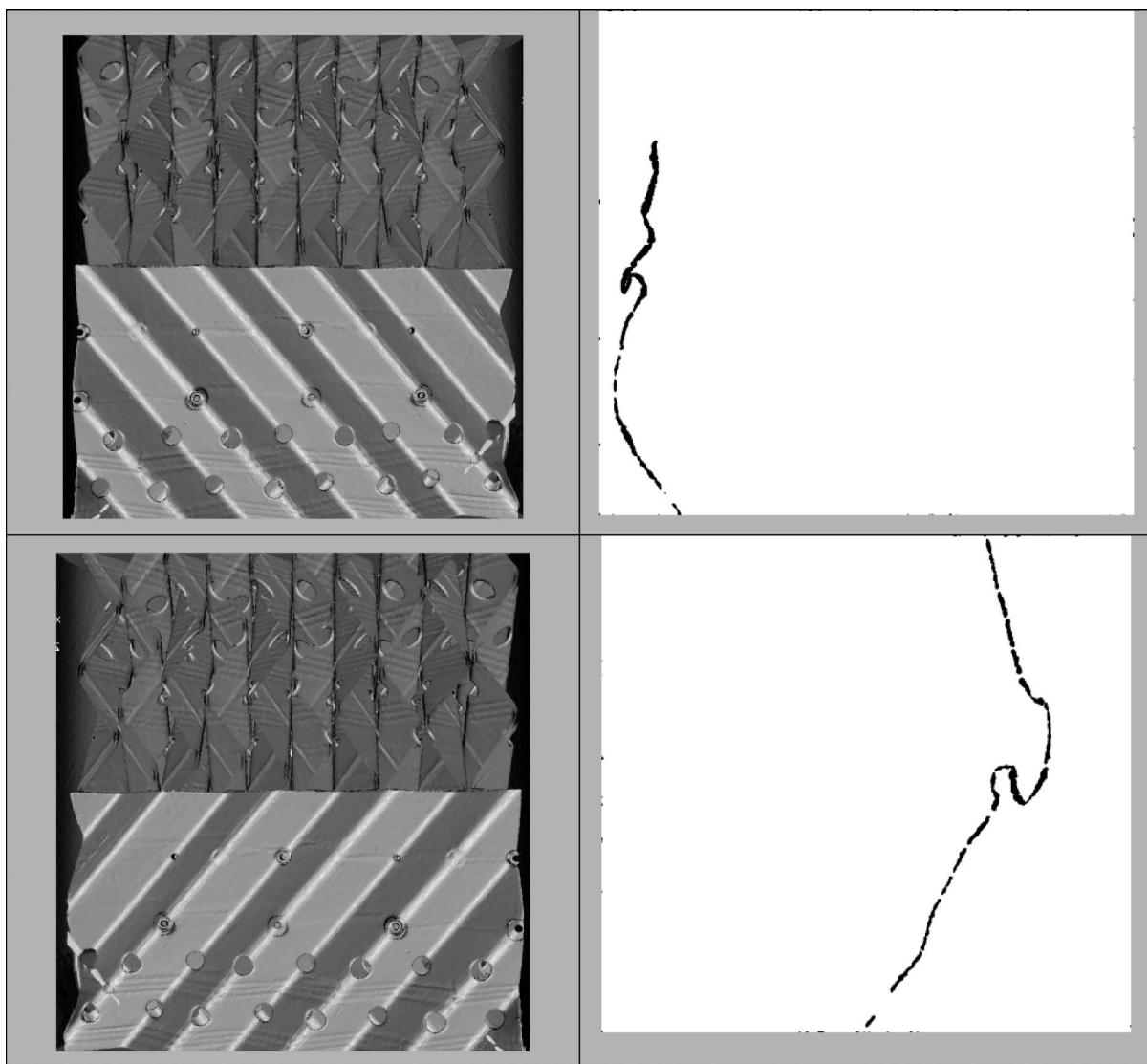


**Figure 24.** Tenth (top) and eleventh (bottom) experiments showed particles reverse flow and seemingly pass under a packing sheet. Shown is flow through the lowest packing joint at  $7.95 \text{ m}^3/\text{hr}$  [35 gpm].

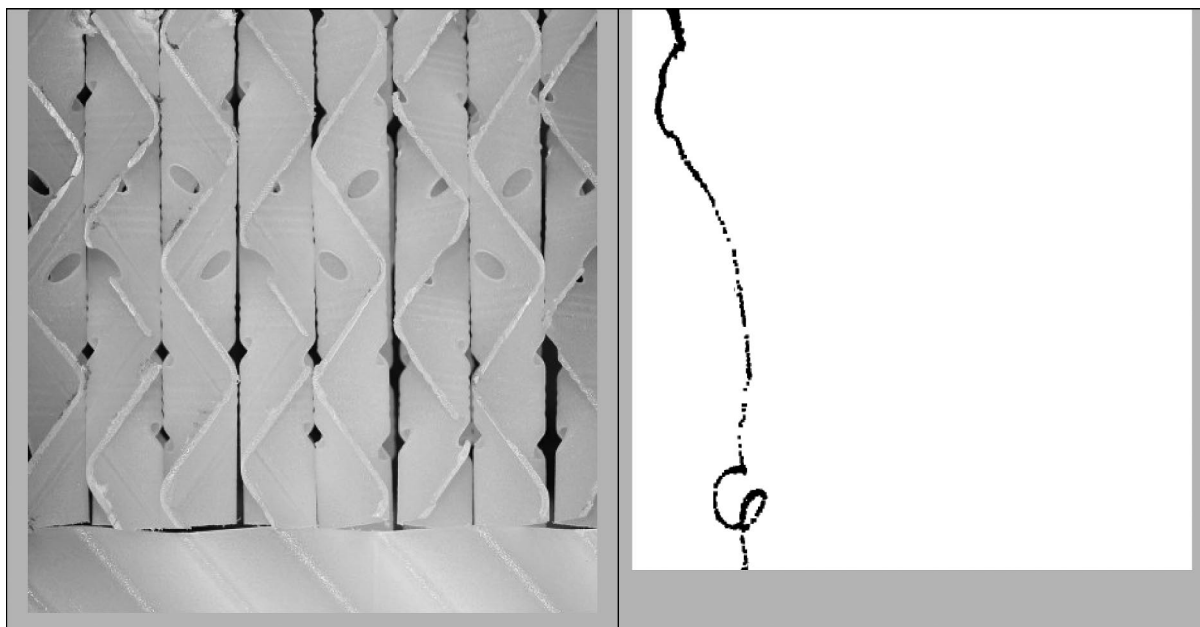


**Figure 25.** Recirculation zones were observed at the joint between packing elements.

the path once it is past the joint, which further supports the belief that little flow disruption occurs within the packing elements.

## 6. Conclusions

The experimental method was successful in capturing both qualitative and quantitative flow field information inside contacting equipment without optical access. This information is crucial to both focused development of new packing designs as well as validation of existing computational models. The method described above does not suffer from the need to modify equipment for optical access, and the size of the equipment is only limited by the power of the X-ray source and size of the detector. This allows the method to be applied more quickly and to a wider range of processing equipment than previous PTV experiments.

The qualitative information captured in this experiment shows that flow within packing elements is largely undisturbed and characterized by linear paths in a single channel. Transitions between adjacent channels were abrupt but smooth and produced little flow disruption. By contrast, flow at the joints was characterized by macro scale recirculation and poor flow integration (wall flow). Improvements in these areas will yield improved contacting and decreased energy intensity. Identifying these features allows packing manufacturers to focus improvements in these areas, which will advance packing designs at an accelerated rate.

The quantitative information was shown to accurately reflect the average interstitial velocities. This suggests that the local flow information captured is representative of the velocity variation throughout the packing. This data can be immediately compared to vapor phase flow physics predicted by existing CFD models. Validation of existing models is required for computer aided design of packing to replace extensive and expensive prototyping. The adoption of a CAD method would allow for a reduced research costs and a shorter time to market as well as enhanced performance.

## 7. Future Work

The recording method employed here was highly dependent on human reaction time and resulted in several missed opportunities. A more advanced system that recorded in real time and used a motion sensor to identify particles and start recording would greatly improve the quality of data obtained by this type of experiment. A greater recording time and particle density would also increase the amount of data obtained in each run. The sampling rate employed was adequate to capture most detail of the particle trajectories. However, the very small scale recirculation and apparent dead zones proved hard to interpret with 30 Hz data. A higher sample rate would allow for more accurate velocity determination across the board and yield more detail near the packing joints where small displacement and repeated paths (recirculation) were observed.

## Acknowledgment

The authors would like to thank Ben Nightingale and Al Berger of the GE Aviation Manufacturing & Quality Technology

Department located in Cincinnati, Ohio. Financial support from the National Science Foundation is gratefully acknowledged. Furthermore, the authors acknowledge Chris Burns and the Texas Advanced Computing Center (TACC) at The University of Texas at Austin for providing visualization resources and support that have contributed to the research results reported within this article. URL: <http://www.tacc.utexas.edu>. The co-operation of Sulzer ChemTech in supplying the packing was instrumental in performing this research.

## Literature Cited

- (1) Durst, F.; Melling A.; Whirelaw J. H. *Principles and Practice of Laser-Doppler Anemometry*; London: Academic Press Inc, 1976.
- (2) Hamed, A.; Malak M. LDV Measurements of Three-Dimensional Flow Development in a Curved Rectangular Duct with Inlet Shear Profile. In *American Institute of Aeronautics and Astronautics, Fluid Dynamics, Plasma Dynamics, and Lasers Conference*; Snowmass: CO, 1984.
- (3) Mazumder, M. K.; et al. Skin friction drag measurements by LDV. *Appl. Opt. Applied Optics* **1981**, *20* (16), 2832–2837.
- (4) Otute Akiki, P. M. A. Experimentally-validated micromixing-based CFD model for fed-batch stirred-tank reactors. *AICHE J.* **2004**, *50* (3), 566–577.
- (5) Hague, J.; et al. Small scale model for CFD validation in DAF applicatoins. *Water Sci. Technol.* **2001**, *43* (8), 167–73.
- (6) Ohmi, K.; Li, H.-Y. Particle-tracking velocimetry with new algorithms. *Meas. Sci. Technol.* **2000**, *11* (6), 603–616.
- (7) Cowen, E. A.; et al. A hybrid digital particle tracking velocimetry technique. *Exp. Fluids* **1997**, *22* (3), 199–211.
- (8) Okamoto, K. Particle cluster tracking algorithm in particle image velocimetry. *JSME International Journal. Series B, Fluids and Thermal Engineering* **1998**, *41* (1), 151–4.
- (9) Barker, J. M. and Liburdy, J. A. *Experimental design considerations for pulsed holographic particle-tracking velocimetry*. Proceedings of the SPIE - Optical Diagnostics in Fluid and Thermal Flow, 1993.
- (10) Veber, P.; Dahl, J.; Hermansson, R. Study of the phenomena affecting the accuracy of a video-based Particle Tracking Velocimetry technique. *Exp. Fluids* **1997**, *22* (6), 482–8.
- (11) Ketcham, R. A.; Carlson, W. D. Acquisition, optimization and interpretation of X-ray computed tomographic imagery: Applications to the geosciences. *Computers & Geosciences* **2001**, *27* (4), 381–400.
- (12) Green, C. W.; et al. *Novel Application of X-ray Computed Tomography: Determination of Gas/Liquid Contact Area and Liquid Holdup in Structured Packing*. *Ind. Eng. Chem. Res.* **2007**, *46* (17), 5734–5753.
- (13) Kertzschner, U.; et al. X-ray based measurements of the local solid phase content in a three-phase flow of a bubble column: Statistical significance. *Exp. Fluids* **2004**, *37* (6), 923–928.
- (14) Kertzschner, U.; et al. X-ray based particle tracking velocimetry-a measurement technique for multi-phase flows and flows without optical access. *Flow Measurement and Instrumentation* **2004**, *15* (4), 199–206.
- (15) Seeger, A.; et al. X-ray-based flow visualization and measurement: Application in multiphase flows. *Ann. N.Y. Acad. Sci.* **2002**, *972* (1), 247–253.
- (16) Seeger, A.; et al. *X-ray-based assessment of the three-dimensional velocity of the liquid phase in a bubble column*. *Experiments in Fluids* **2001**, *31* (2), 193–201.
- (17) Seeger, A.; et al. Measurement of the local velocity of the solid phase and the local solid hold-up in a three-phase flow by X-ray based particle tracking velocimetry (XPTV). *Chem. Eng. Sci.* **2003**, *58* (9), 1721–1729.
- (18) Awcock, G. W.; Thomas R. *Applied Image Processing*; McGraw-Hill: New York, NY, 1996; p 300.
- (19) Bovik, A. *Handbook of Image and Video Processing*, 2nd ed.; Elsevier Academic Press: Burlington, MA, 2005; p 1372.

Received for review August 18, 2008  
Revised manuscript received January 11, 2009

Accepted January 19, 2009

IE801260S